Monthly Notices of the ROYAL ASTRONOMICAL SOCIETY

MNRAS **514,** 3670–3684 (2022) https://doi.org/10.1093/mnras/stac1543
Advance Access publication 2022 June 16

The signature of large-scale turbulence driving on the structure of the interstellar medium

Tine Colman [1]★ Jean-François Robitaille [2] Patrick Hennebelle,[1] Marc-Antoine Miville-Deschênes,[1] Noé Brucy [1] Ralf S. Klessen [3,4] Simon C. O. Glover [3] Juan D. Soler,[5] Davide Elia,[5] Alessio Traficante [5] Sergio Molinari[5] and Leonardo Testi[6,7]

[1] *Université Paris Saclay and Université de Paris, CEA, CNRS, AIM, F-91190 Gif-sur-Yvette, France*
[2] *Univ. Grenoble Alpes, CNRS, IPAG, F-38000 Grenoble, France*
[3] *Universität Heidelberg, Zentrum für Astronomie, Institut für Theoretische Astrophysik, Albert-Ueberle-Str 2, D-69120 Heidelberg, Germany*
[4] *Universität Heidelberg, Interdisziplinäres Zentrum für Wissenschaftliches Rechnen, Im Neuenheimer Feld 205, D-69120 Heidelberg, Germany*
[5] *INAF - Istituto di Astrofisica e Planetologia Spaziali, via Fosso del Cavaliere 100, I-00133 Roma, Italy*
[6] *European Southern Observatory, Karl-Schwarzschild-Str. 2, D-85748 Garching bei München, Germany*
[7] *INAF - Osservatorio Astrofisico di Arcetri, Largo E. Fermi 5, I-50125 Firenze, Italy*

Accepted 2022 May 31. Received 2022 April 15; in original form 2022 January 31

ABSTRACT

The mechanisms that maintain turbulence in the interstellar medium (ISM) are still not identified. This work investigates how we can distinguish between two fundamental driving mechanisms: the accumulated effect of stellar feedback versus the energy injection from galactic scales. We perform a series of numerical simulations describing a stratified star-forming ISM subject to self-consistent stellar feedback. Large-scale external turbulent driving, of various intensities, is added to mimic galactic driving mechanisms. We analyse the resulting column density maps with a technique called Multi-scale non-Gaussian segmentation, which separates the coherent structures and the Gaussian background. This effectively discriminates between the various simulations and is a promising method to understand the ISM structure. In particular, the power spectrum of the coherent structures flattens above 60 pc when turbulence is driven only by stellar feedback. When large-scale driving is applied, the turn-over shifts to larger scales. A systematic comparison with the Large Magellanic Cloud (LMC) is then performed. Only 1 out of 25 regions has a coherent power spectrum that is consistent with the feedback-only simulation. A detailed study of the turn-over scale leads us to conclude that regular stellar feedback is not enough to explain the observed ISM structure on scales larger than 60 pc. Extreme feedback in the form of supergiant shells likely plays an important role but cannot explain all the regions of the LMC. If we assume ISM structure is generated by turbulence, another large-scale driving mechanism is needed to explain the entirety of the observations.

Key words: turbulence – ISM: structure – galaxies: Magellanic Clouds.

1 INTRODUCTION

It has become clear that turbulence plays an important role in the star formation process (see e.g. the reviews of Elmegreen & Scalo 2004; Mac Low & Klessen 2004; McKee & Ostriker 2007; Hennebelle & Falgarone 2012; Klessen & Glover 2016). Compressible supersonic turbulence generates a complex network of shocks and filaments as seen in observation of the interstellar medium (ISM). Because turbulence naturally dissipates on small scales, a form of driving at larger scales is needed to maintain the turbulent kinetic energy in the system. The regime between the injection scale and the dissipation scale is called the inertial range and contains fully developed turbulence (see e.g. Lesieur 2008). Stellar feedback in the form of supernovae (SN), jets, winds, and ionizing radiation has been shown to be an important driving mechanism (Avillez & Breitschwerdt 2005; Joung & Mac Low 2006; Kim, Ostriker & Kim 2013; Girichidis et al. 2016; Padoan et al. 2016; Iffrig & Hennebelle 2017). These processes shape the structure of the ISM and can sometimes completely destroy the molecular clouds that are the formation sites of the stars.

Bubbles blown by the feedback of a single massive star have typical sizes of a few tens of parsecs. When multiple massive stars form in close proximity, bubbles can combine to form structures with sizes of the order of 100 pc (Chu 2008). Stellar feedback injects energy and momentum into the ISM on the scales of individual stars and their feedback bubbles (Walch et al. 2015; Girichidis et al. 2016). Another mechanism for driving turbulence, which is much less investigated, is the energy cascade from larger scales, i.e. the galactic scale, to the molecular cloud scale (Klessen & Hennebelle 2010). It has been shown that global galactic motions can indeed drive the turbulence on scales larger than 1 kpc (Wada 2008; Bournaud et al. 2010; Renaud, Kraljic & Bournaud 2012; Krumholz et al. 2018; Meidt et al. 2018; Nusser & Silk 2022). The energy injected on these large scales then cascades further down and provides turbulent energy on smaller scales. Although the properties of turbulence in the inertial range

★ E-mail: tine.colman@cea.fr

do not depend on the injection mechanism, we can still expect these different driving mechanisms to alter the structure and properties of the ISM in different ways. In particular, the scales which are of the order of the injection scale can carry signatures of the driving mechanism.

It is currently unknown how important large-scale driving is for star formation and what imprint it leaves on the structure of the ISM. In a previous study, Brucy et al. (2020) investigated the effect of external driving on the star formation rate (SFR) in the context of high column density regions. These simulations showed that strong external driving is needed to quench the star formation and obtain the correct slope for the observed Kennicutt–Schmidt relation (Kennicutt & Evans 2012), which correlates the SFR with the gas column density of the star-forming region. In this work, we study another aspect of large-scale driving, i.e. the structure of the ISM. We focus on the global structure in systems with characteristics typical of present-day galaxies. The properties of substructures, such as molecular clouds and star clusters, will be addressed in a future paper.

For the purpose of this study, we run a suite of simulations representing a 1 kpc part of a galactic disc. The simulations, which are presented in detail in Section 2, include a large range of physics, including stellar feedback and various external driving strengths. The external driving is applied on scales of a 1/3, 1/2, and a full box length, significantly larger than the size of a typical stellar feedback bubble. We analyse the final ISM structure and look for observable signatures of large-scale driving. The tool we use in this work is called Multi-scale non-Gaussian segmentation (MnGseg) and is described in Robitaille, Joncas & Miville-Deschênes (2014) and Robitaille et al. (2019), as well as in Section 3. According to Falgarone, Hily-Blant & Levrier (2004), the ISM can be decomposed into two components: a Gaussian fluffy fractal component and a component containing the dense structures such as cores and filaments. MnGseg can separate these two components, dubbed Gaussian and coherent, allowing us to study their individual characteristics. The diagnostic we are particularly interested in is the power spectrum (PS), which quantifies the amount of structure as a function of spatial scale. Indeed, the column density PS has been used in many observational and theoretical papers to characterize the ISM (see e.g. Kritsuk et al. 2007; Miville-Deschênes et al. 2007; Federrath et al. 2010a; Federrath & Klessen 2013; Schneider et al. 2015). In this work, rather than measuring the classical Fourier PS, MnGseg uses a wavelet-based method. It turns out that the PS of the separated components (Gaussian and coherent) carries, for our purpose, more information than the total PS, as is demonstrated in Section 4 where we apply this technique to the simulation results. Since MnGseg has never been applied to simulations before, we perform a series of tests that helps us to determine what algorithm parameters are most suited, how to interpret the results, and how we can best compare with observation.

Once we have identified the signature of large-scale driving on the PS decomposition, we can look for it in observations. For this, we apply MnGseg to Herschel 500 μm observations of the Large Magellanic Cloud (LMC). We need an external galaxy for this type of analysis, and the LMC provides the best target since it is close-by and face-on, which means we can study a large range of scales. The results of this are described in Section 5. The statistical properties of the LMC have been studied by many authors (e.g. Elmegreen, Kim & Staveley-Smith 2001; Szotkowski et al. 2019; Koch et al. 2020). However, a decomposition, as done by MnGseg, has not yet been attempted. In fact, so far, MnGseg has only been applied on regions much smaller than 1 kpc. Using the insights gained from the simulations as means to interpret the observations, we determine whether large-scale driving might play an important role.

Finally, in Section 6, we discuss the results and caveats. After obtaining clues from local variation within the LMC, we speculate about the possible sources of large-scale driving. Note that the LMC is not only convenient because it is close-by. It also has interesting features that are candidates for large-scale driving sources: it has large-scale stellar structures in the form of spiral arm(s) and a bar, and it is tidally interacting with the Milky Way and Small Magellanic Cloud (SMC). If we find evidence that any of these can inject turbulence from large scales into the ISM of the LMC, we could expect them to play a role in other galaxies as well. This, of course, should then be verified by dedicated studies of other galaxies.

We end the paper with a summary of our conclusions.

2 SIMULATION SETUP

The simulation setup is similar to the ones used in previous works (Iffrig & Hennebelle 2015; Colling et al. 2018; Brucy et al. 2020), however, in this study we allow for deeper adaptive mesh refinement up to a minimum cell size of 0.24 pc. This allows us to more accurately study the morphological and dynamical properties of dense interstellar structures.

2.1 Initial conditions

We model a 1 kpc part of a galactic disc. Initially, the density profile along the z-axis is given by a Gaussian

$$n(z) = n_0 \exp\left[-\frac{1}{2}\left(\frac{z}{z_0}\right)^2\right] \tag{1}$$

with n_0 the mid-plane density and z_0 the thickness of the disc. We adopt $n_0 = 1.5\,\mathrm{cm}^{-3}$ and $z_0 = 150$ pc corresponding to a gas column density of 19.1 $\mathrm{M}_\odot\ \mathrm{pc}^{-2}$, a value which is slightly higher than the average value found in the LMC but in good agreement with dense sub-regions [as can be inferred from the data presented in Kim et al. (2003) and Wong et al. (2011)]. This profile is embedded in an external gravitational potential of the form

$$g(z) = -\frac{a_1 z}{\sqrt{z^2 + z_0^2}} - a_2 z \tag{2}$$

with $a_1 = 1.42 \times 10^{-3}$ kpc Myr^{-2}, $a_2 = 5.49 \times 10^{-4}\,\mathrm{Myr}^{-2}$, and $z_0 = 0.18$ kpc (Kuijken & Gilmore 1989; Joung & Mac Low 2006). Self-gravity is also considered. An initial level of turbulence is introduced by adding a turbulent velocity field with a rms dispersion of 5 km s^{-1} and a Kolmogorov PS $E(k) \propto k^{-5/3}$ with random phase. The initial temperature is 5333 K, which is a typical value for the warm neutral medium phase in the ISM. We also include an initial Gaussian magnetic field with an orientation along the x-axis

$$B_x(z) = B_0 \exp\left[-\frac{1}{2}\left(\frac{z}{z_0}\right)^2\right] \tag{3}$$

with $B_0 = 7.62\,\mu\mathrm{G}$, comparable to the field strength in the Milky Way and LMC (Gaensler et al. 2005; Hassani et al. 2022). The box is periodic in the x- and y-direction and has open boundary conditions in the z-direction.

2.2 Numerics

To evolve our simulation in time, we use the ISM version of the adaptive mesh refinement hydrodynamics code RAMSES (Teyssier 2002), with a treatment of the magnetic field using ideal magnetohydrodynamics (Fromang, Hennebelle & Teyssier 2006) and

radiation using the M1 method (Rosdahl et al. 2013). Cooling is as described in Audit & Hennebelle (2005). We also include heating from a uniform ultraviolet background with strength equal to the solar neighbourhood field.

The coarse grid has a resolution of 3.9 pc (refinement level[1] 8). The grid is then refined further when a cell exceeds a certain mass,[2] up to level 12 corresponding to a maximum resolution of 0.24 pc in the densest regions. We introduce sink particles (Bate, Bonnell & Price 1995; Federrath et al. 2010b) when the gravitational collapse reaches the resolution limits, which mimics the formation of a star cluster and helps to prevent singularities in the computational domain. We use the sink formation algorithm from Bleuler & Teyssier (2014). Sinks are created from overdensities identified by the native RAMSES clumpfinder (Bleuler et al. 2015) if their density exceeds the threshold of 10^4 H cm^{-3}. Additionally, this implementation checks that the gas clump from which the sink is forming is collapsing and bound. After their birth, sinks accrete gas according to the threshold accretion scheme: only gas which is above the sink formation threshold and within the accretion radius of four cells will be accreted, with a maximum of 75 per cent of the mass available per time step. No additional checks are applied before the gas is accreted. New sinks cannot form within the accretion radius of existing sinks. Sinks are not allowed to merge. All simulations have been run for 60 Myr during which 2–5 per cent (depending of the simulations) of the gas has been converted into stars. After this time, the turbulence is fully developed as shown in Appendix D.

2.3 Stellar feedback

Sink particles also serve as a source of stellar feedback. Each time a sink has accreted a mass of 120 M$_\odot$, a massive star particle with a mass randomly determined from the Salpeter IMF (Salpeter 1955) between 8 and 120 M$_\odot$ is created. We associate a lifetime τ_* with this star using the model

$$\tau_*(M) = \tau_0 \exp\left[-a\left(\log\left(\frac{M}{M_0}\right)\right)^b\right] \tag{4}$$

with $\tau_0 = 3.265$ Myr, $M_0 = 148.16$ M$_\odot$, $a = 0.238$, and $b = 2.205$ (Woosley, Heger & Weaver 2002). Once this massive star has reached the end of this lifetime, it explodes in a random location within a sphere of radius $\tau_* \times 1$ km s^{-1}. Given the typical lifetimes of massive stars, this can range from a fraction of a parsec to about 30 pc. The explosion injects a momentum of roughly 4×10^{43} g cm s^{-1} (but no thermal energy) into the ISM (Iffrig & Hennebelle 2015), mimicking a supernova.

We also include self-consistent feedback from H II regions, with energy and momentum injected according to the flux of ionizing photons emitted by the star. The evolution of H II regions itself is computed by the radiative transfer module of RAMSES (Rosdahl et al. 2013), as in Geen et al. (2016). For details about the exact implementation, see Colling et al. (2018) and references therein.

Due to their computational cost, we do not include stellar winds.

[1]When refined, the cell is divided by 2 along each spatial axis. The refinement level indicates how many times this division is done.

[2]The thresholds are 5.7×10^{-4}, 7.1×10^{-4}, 4.4×10^{-4}, and 1.1×10^{-4} M$_\odot$.

2.4 External driving

In this work, we study the effect of turbulent energy injection from large scales. A turbulence driving force is added as an additional external force in the Euler equation. The Fourier modes of this force are computed using the generalized Ornstein–Uhlenbeck process and follow a stochastic differential equation:

$$\mathrm{d}\vec{F}(\vec{k},t) = F_0\left(\vec{k}\right)\vec{P}\begin{pmatrix}k_x\\k_y\\0\end{pmatrix}\mathrm{d}\vec{W}_t - \vec{F}(\vec{k},t)\frac{\mathrm{d}t}{T} \tag{5}$$

(Eswaran & Pope 1988; Schmidt, Niemeyer & Hillebrandt 2006; Schmidt et al. 2009). The first term describes a stochastic contribution to the force. $\vec{F}$ is a complex 3D vector in Fourier space. F_0 is the PS assigning a weight to each $\vec{k}$-mode. In this study, we drive on scales between 1 box length and 1/3 of the box length with a parabolic PS

$$F_0\left(\vec{k}\right) = \begin{cases} 1-(|k|-2)^2 \text{ if } 1 < |k| < 3 \text{ and } k_x > 0 \text{ and } k_y > 0 \\ 0 \text{ otherwise} \end{cases} \tag{6}$$

which peaks at scales of half the box size. The purely vertical modes are removed. $\vec{P}(\vec{k})$ is the projection operator that takes care of compressive versus solenoidal modes through a Helmholtz decomposition. It is defined as

$$\vec{P}\left(\vec{k}\right) = \zeta\vec{P}^{\perp}\left(\vec{k}\right) + (1-\zeta)\vec{P}^{\parallel}\left(\vec{k}\right) \tag{7}$$

with $\vec{P}^{\perp}$ and $\vec{P}^{\parallel}$ the projection operators, respectively perpendicular and parallel to $\vec{k}$ (Federrath et al. 2010b). For the solenoidal fraction ζ, we choose $\zeta = 0.75$. This is higher than the standard value of 0.5 for a natural mix (Federrath, Klessen & Schmidt 2008). However, Jin et al. (2017) find that in their galaxy simulations the velocity field is mainly solenoidal, which may hint that turbulence driving by galactic dynamics might be dominantly solenoidal. Because our setup is a stratified disc, the projection is done on to the 2D plane of the disc [the projection operator $\vec{P}$ is applied to $(k_x, k_y, 0)$ instead of $\vec{k}$ in equation (5)]. $\mathrm{d}\vec{W}_t$ is the Wiener process, which gives us a random vector from a Gaussian distribution with zero mean and variance. $\mathrm{d}t$ is the time step of integration. The second term is an exponential decay with T the autocorrelation time, which is set to $T = 40$ Myr.

Once the Fourier modes $\vec{F}$ are calculated, they are converted into a real force by applying a Fourier transform. The force is then multiplied by a boost factor $f_{\rm rms}$ to adjust its strength, measured through the time average of the rms value of the Fourier coefficients:

$$\mathrm{RMS} = \left\langle f_{\rm rms}\sqrt{\int\left|\vec{F}(\vec{k},t)\right|^2\mathrm{d}^3\vec{k}}\right\rangle_t, \tag{8}$$

where $<\cdot>_t$ denotes the time average.

The parameters that characterize the turbulence driving are the boost factor (which sets the RMS value of equation 8), the autocorrelation time, the PS of the modes, and the solenoidal fraction. In this study, we vary the driving strength while keeping the other parameters constant. We take boost factors $f_{\rm rms}$ of 3000, 6000, and 24 000, corresponding to weak, medium, and strong driving, respectively. For completeness, the corresponding values for the RMS are listed in Table 1. These parameters values correspond to three different final velocity dispersions and have been chosen through experimentation. The energy injection for each driving strength is listed in Table 1 and will be discussed in Section 4.2. We also run a simulation without driving. This allows us to separate the effects of driving by stellar feedback from those of external large-scale driving.

Table 1. Estimates of the total energy injected by SN and external turbulence driving during each simulation. E_{SN} is estimated as the number of supernovae times 10^{51} erg times an efficiency ε. The definitions of f_{rms} and RMS are given in equation (8). The last column shows the final mass-weighted velocity dispersion within the disc (defined as the region within 200 pc above and below the mid-plane).

Driving	f_{rms}	RMS (km s^{-1} Myr^{-1})	E_{turb} (10^{51} erg)	E_{SN} (10^{51} erg) (ε = 2–10 per cent)	$\sigma_{3D}(t = t_{end})$ (km s^{-1})
None	0	0	–	40–204	8.49
Weak	3000	0.27	144	50–254	9.08
Medium	6000	0.54	578	66–329	12.06
Strong	24 000	2.08	5905	46–229	20.13

3 MULTISCALE NON-GAUSSIAN SEGMENTATION

The MnGseg analysis was developed by Robitaille et al. (2014, 2019) and is inspired by the analysis of turbulent fluid flows of Nguyen van yen, Farge & Schneider (2012). The implementation is freely available as the PYTHON package PYWAVAN.[3] For a detailed prescription, we refer to the above mentioned works. Here, a short summary is given. For the sake of readability and conciseness, most of the technical details and several illustrative figures are provided in Appendix A.

3.1 Wavelet power spectrum

Structures with a certain size and orientation can be identified in an image $f(\vec{x})$ by convolving it with a complex Morlet wavelet of size ℓ and orientation angle θ (Robitaille et al. 2014). The convolution operation for the wavelet transform is done in the Fourier space,

$$\tilde{f}_{\ell,\theta}(\vec{x}) = \mathcal{F}^{-1}\left\{\hat{f}\left(\vec{k}\right)\hat{\psi}^{*}_{l,\theta}\left(\vec{k}\right)\right\} \tag{9}$$

where $\mathcal{F}^{-1}$ denotes the inverse Fourier transform, and $\hat{f}(\vec{k})$ and $\hat{\psi}_{\ell,\theta}(\vec{k})$ denote, respectively, the Fourier transform of the image and of the Morlet wavelet $\psi_{\ell,\theta}(\vec{x})$. Fig. A1 illustrates the resulting wavelet coefficients $\tilde{f}_{\ell,\theta}$ for three different sizes and angles. To calculate the total wavelet PS $P(\ell)$, one simply averages the squared absolute value of the complex wavelet coefficients over angles (Fig. A2) and then over spatial coordinates $\vec{x}$:

$$P(\ell) = \left\langle |\tilde{f}_{\ell,\theta}(\vec{x})|^2 \right\rangle_{\theta,\vec{x}} \tag{10}$$

as illustrated in Fig. A3. Equation (10) calculates the second-order moments of wavelet coefficients. It can be shown that using the complex Morlet wavelet, this measurement becomes equivalent to the standard Fourier PS analysis (Robitaille et al. 2019; Kirby 2005) as can be seen in Fig. A3.

We can estimate the error on the wavelet PS in a way similar to what is done for the Fourier PS. The number of times a wavelet of size ℓ fits into the domain sets the number of samples $S(\ell) = L/\ell$ for that scales, where L is the size of the full domain. The larger ℓ, the smaller S and the larger the error. Analogous to the Fourier PS, we define the error due to limited sampling as

$$\text{error}(\ell) = \frac{P(\ell)}{S(\ell)} \tag{11}$$

For a domain that spans 1 kpc, this results in an error of less than 20 per cent for scales below 200 pc.

[3] https://github.com/jfrob27/pywavan

3.2 Decomposition into Gaussian and coherent part

Once we have the convolved images, through an iterative process as a function of ℓ and θ, MnGseg separates the Gaussian and coherent component. The fractal Gaussian part is, as its name suggests, associated with a Gaussian signal in the image. Plotting the histogram of wavelet coefficients $\tilde{f}_{\ell}(\vec{x})$ of an originally fractal image results in self-similar Gaussian distributions at every scale. Note that depending on the power law of $P(\ell)$, the total image with all integrated spatial scales is not necessary Gaussian. In complex systems like the ISM, many physical processes shape the structure, introducing clumps, filaments, and bubbles. The presence of these 'coherent' structures will alter the distribution by adding a non-Gaussian component. In other words, if one can identify and remove the Gaussian component, whatever remains are coherent structures. The procedure MnGseg follows to separate the two components is to count the high intensity tail in the distribution as coherent. This segmentation is illustrated in Fig. A5.

The segmentation procedure introduces a segmentation parameter q to regulate how strict we want our Gaussian distribution to be. Gaussianity is evaluated on the absolute value of the complex Morlet wavelet coefficients $|\tilde{f}_{\ell,\theta}(\vec{x})|$. Consequently, the coefficient distributions correspond to Rician distributions, rather than a pure Gaussians, and a small skewness is expected. This q parameter is involved in the iterative process used to converge to the best threshold Φ (Nguyen van yen et al. 2012):

$$\begin{cases} \Phi_0(l,\theta) = \infty \\ \Phi_{n+1}(l,\theta) = q\,\sigma_{l,\theta}(\Phi_n), \end{cases} \tag{12}$$

where $\sigma_{l,\theta}(\Phi_n)$ is defined as,

$$\sigma^2_{l,\theta}(\Phi) = \frac{1}{N_{l,\theta}(\Phi)} \sum_{\vec{x}} \mathbb{L}_{\Phi}\left(|\tilde{f}_{l,\theta}(\vec{x})|\right) |\tilde{f}_{l,\theta}(\vec{x})|^2, \tag{13}$$

with

$$\mathbb{L}_{\Phi}\left(|\tilde{f}_{l,\theta}(\vec{x})|\right) = \begin{cases} 1 & \text{if} \quad |\tilde{f}_{l,\theta}(\vec{x})| < \Phi \\ 0 & \text{else,} \end{cases} \tag{14}$$

and

$$N_{l,\theta}(\Phi) = \sum_{\vec{x}} \mathbb{L}_{\Phi}\left(|\tilde{f}_{l,\theta}(\vec{x})|\right). \tag{15}$$

Choosing a large value for q will result in a large fraction of the signal being counted as Gaussian, as the cut-off for coherent structures shifts to larger, more extreme values of $|\tilde{f}_{l,\theta}|$. On the other hand, choosing a small q will categorize almost all values of $|\tilde{f}_{l,\theta}|$ as coherent structure. MnGseg can optimize the dimensionless parameter q for each individual scale by measuring the skewness of the coefficient distributions and iterating until a desired skewness is obtained. After many experiments, we settled on a fixed $q = 2$, a value in line with what is expected from a theory (Nguyen van yen et al. 2012) and comparable to what is used in previous studies (Robitaille et al. 2019, Cunningham et al. in preparation). Where instructive, we show

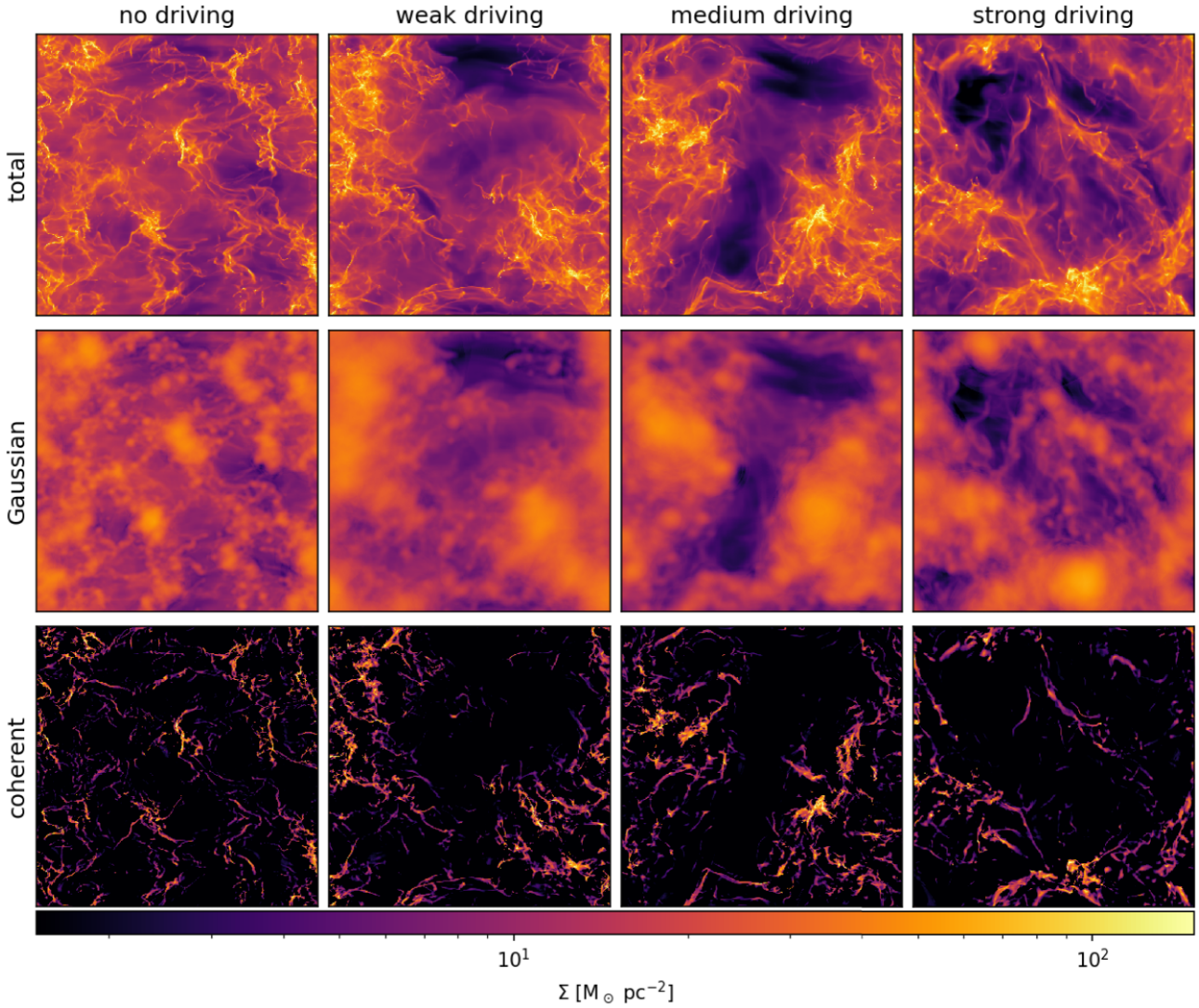

Figure 1. MnGseg applied on the face-on view at the end of the simulations ($t_{\rm end} = 60$ Myr). Each images spans the full 1 kpc^2 of the simulation box. Top: the original image, middle: Gaussian component of the image (including average), and bottom: coherent component (excluding average) of the image. The total image is the sum of the Gaussian and the coherent part.

results obtained with a different values. The segmentation obviously depends on the adopted value of q. However, when we apply MnGseg on several different data sets using the same q for all data, the resulting relative differences between data sets remains largely independent on the adopted value of q. This seemingly indicates the validity and robustness of the conclusions (see Appendix B and Section 4.1).

3.3 Application to simulations

Whereas in principle the segmentation can be performed on the full 3D data cube, the observations we want to compare to are inherently 2D projections of the sky, so we will limit ourselves to analysing projections of the density field of our simulations. The face-on projection lends itself excellently to this task, since it has periodic boundaries, avoiding any artefacts that may result from Fourier transforming a non-periodic image. To analyse the edge-on views, we could select only a part of the disc. These regions would be of a size determined by the thickness of the disc, which is about 250 pc. However, since the external driving we chose in our setup operates on scales between 1 kpc and 333 pc, its signature is likely to be difficult to capture in images of regions smaller than the injection scale. Another reason to focus on the face-on views is that it is fairly straightforward to compare with face-on external galaxies. When looking at edge-on galaxies, the sight line is much larger than the 1 kpc which is modelled here.

To generate the column density images, we use a wrapper around the AMR2MAP tool provided with RAMSES. The density is projected along the z-axis of the simulation grid on to an array of 1024×1024 pixels. This means that one level 10 cell corresponds to 1 pixel. Contributions from cells that are at higher refinement levels are weighted by their size.

4 SIMULATION RESULTS

4.1 Determining the signature of large-scale driving

We now apply MnGseg to the face-on view of our simulations. Fig. 1 displays the resulting image decomposition. We see that the overdense filaments and clumps are well recovered in the coherent image, whereas the Gaussian image looks like a fluffy fractal cloud,

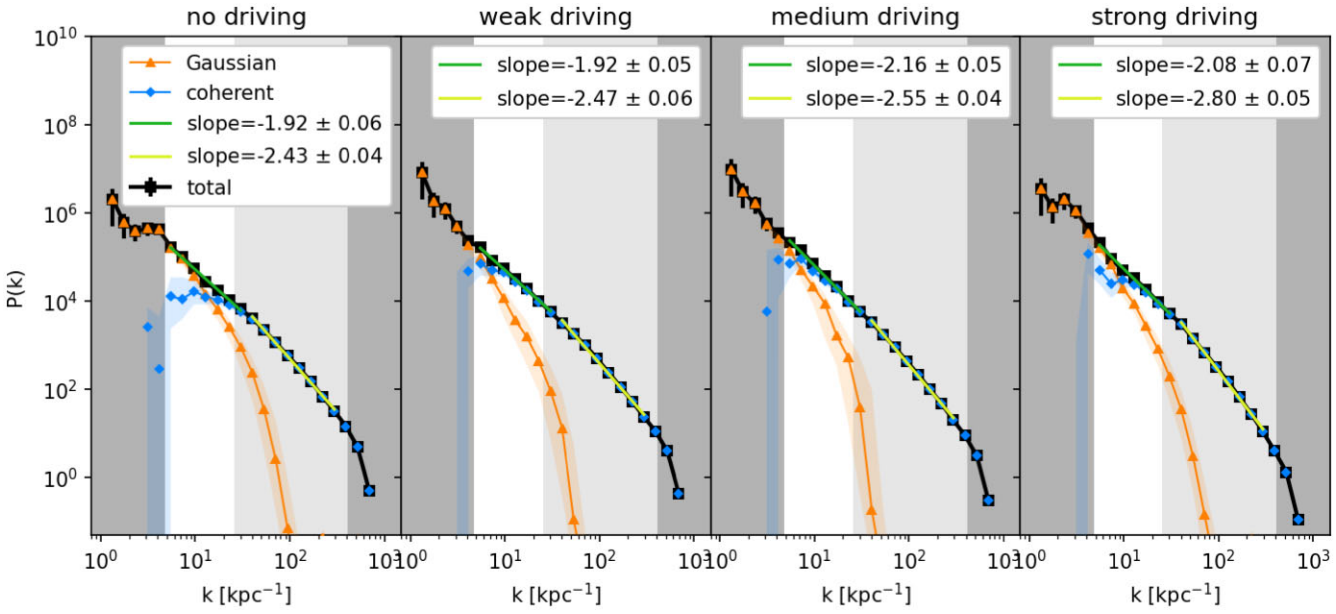

Figure 2. The decomposition of the power spectra into Gaussian and coherent part, corresponding to the density maps of Fig. 1 ($q = 2.0$). The green lines show power-law fits to the total PS. The grey areas mark regions where uncertainties are large due to limited statistics (small k) and limited resolution of the simulation (large k) where the light and dark grey indicates 10 times the coarse grid and fine grid resolution, respectively. The coloured bands show the segmentation results when varying q between 1.8 and 2.2.

as expected. The corresponding power spectra are shown in Fig. 2. The total PS can be described by two power laws: one for large scales in which the diffuse part is well resolved and one for smaller scales, which probe the adaptive mesh refinement region. We fit the slope in both of these regimes. The total PS for the no-driving case and the weak driving case is the same, while in the medium and strong driving case it is slightly steeper. For small scales, there is a trend of steeper slope with increasing driving strength. A similar trend may be present in for large scales, though it is less clear.

When we do the decomposition, the Gaussian component dominates the large scales (small k) and sharply drops at small scales, due to the lack of resolution in the diffuse gas in the simulation, since the mesh is refined only in the dense regions. Comparing the Gaussian PS to the resolution limit for diffuse gas, i.e. 10 times the coarse grid cell size indicated in light grey in the figure, seems to confirm this hypothesis. The coherent part becomes the dominant contribution above a turn-over $k_{\rm LS}$. The associated scale could be interpreted as a maximum coherent structure size which the turbulent driving is able to generate. A clear distinction can be made between the simulations with and without external driving. For the no-driving case, the coherent PS flattens at large scales. In the simulations with driving, the power law continues towards larger scales with a turn-over close to the statistics limit. We define the turn-over scale $\ell_{\rm LS}$ quantitatively as the largest scale where $P_{\rm coherent} > P_{\rm Gaussian}$. Without driving, $\ell_{\rm LS} = 58$ pc. In the weak and medium driving case, this turn-over is shifted to larger scales, with $\ell_{\rm LS} = 137$ pc. For the strong driving, we do not see a clear flattening of the coherent PS, though there is a small dip at 103 pc, roughly at the same scales where the weak and medium coherent PS have their turn-over.

To verify these trends, we repeat the analysis for different times in the simulations and for different values of the segmentation parameter q. A full study of the variations with q can be found in Appendix B.

The right column of Fig. 3 compares the coherent PS at the end of each simulation (60 Myr) for different values of q. For $q = 1.6$, it is difficult to distinguish the simulations, since most of the signal is labelled as coherent. When increasing q, we see the large-scale coherent PS becomes weaker rapidly in the no-driving case. The results for simulations with driving are much less affected by the change in q This means it is more difficult to recover large-scale coherent structure in the no-driving case compared to the simulations with driving. The dashed line shows the result for a simulation with weak driving and a different turbulence driving seed. This reassures us that the location of the turn-over is not a statistical fluctuation caused by the random driving.

One thing that requires some explanation is the dip for the strong driving case, which becomes even more pronounced when increasing q as seen in Fig. 3. To gain some insight, we look at the time evolution. The left part of this figure shows the coherent PS at different times in each simulation. What stands out is that in the no-driving case, there is a clear decrease at large scales over time, which is not observed in the simulations with external driving. What we see here is the imprint of the initial conditions dissipating. As explained in Section 2, we start the simulation with a random turbulent velocity field. This field has large-scale modes, which dissipate as the simulation evolves. In the simulations with external driving, these modes are replenished. Without external driving, they decay. When looking at the time evolution for the strong driving case, there is a a small increase in large-scale power from 40 to 50 Myr, while the dip is developed between 50 and 60 Myr. It is thus likely a statistical fluctuation of the large-scale geometry. This illustrates that the uncertainties on large scales are significant, but everything smaller than 100 pc is well described. This ensures the turn-over observed around 50 pc in the no-driving case is real and no such flattening is observed in the cases with driving until scales which are *at least* twice as large.

In summary, a clear difference can be seen when comparing the coherent PS of the simulation without external driving to the ones with driving. Whether there is a difference between the individual simulations which include driving is debatable. There might be an

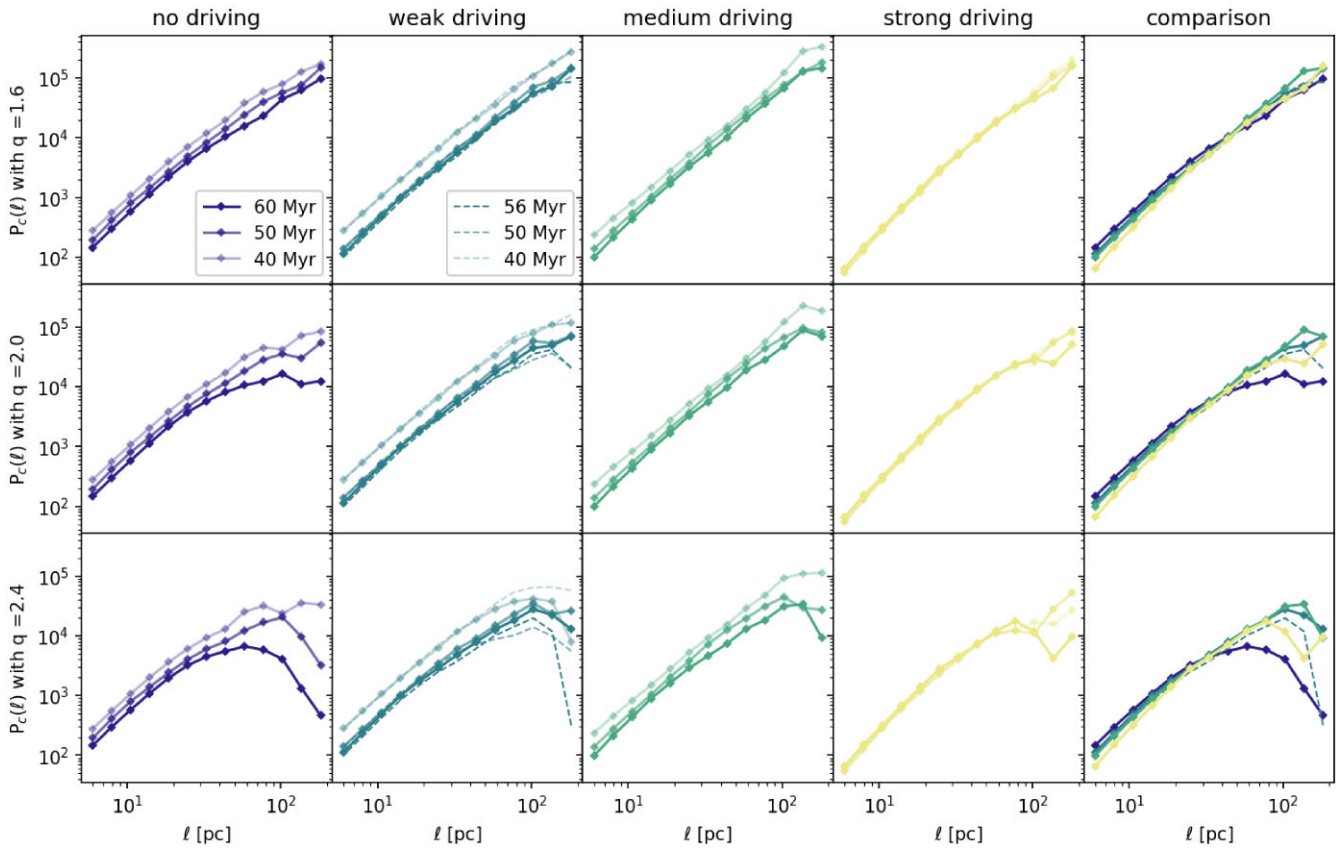

Figure 3. Variation of the coherent part of the PS with segmentation parameter q and time. The dashed line shows the result of a weak driving simulation with a different turbulence driving seed. The right-most column compares the results at the end of the simulations (60 Myr).

indication that stronger driving leads to steeper power spectra, but more data are needed to draw robust conclusions. Overall, this PS analysis confirms what can be seen visually in the column density maps: large-scale external turbulence driving generates large-scale coherent structure in the ISM. The typical size scale of these structures is larger than what can be generated with stellar feedback alone.

4.2 Estimates of the injected energy

One obvious question at this stage is: how much energy is injected from stellar feedback and from external driving?

To answer this question, we compare the energy injected by external turbulent driving to the energy injected by supernova over the course of the simulation. These numbers are shown in Table 1. The energy injected by external driving is directly computed in the simulations, while the energy from the supernovae is simply obtained by multiplying their number by $E_{SN}=10^{51}$ erg, the energy injected by one supernovae, and an efficiency ε. The efficiency of supernova driving turns out to be rather low. Iffrig & Hennebelle (2017), using an analytical model of the galactic scale-height, have estimated this to be on the order of few per cents, possibly as low as 1–2 per cent. This is likely due to several not exclusive facts: (i) supernovae efficiently dissipate their energy; (ii) when they explode in a group or at high latitude, a significant fraction of their energy goes into galactic winds; (iii) supernova explosions have proven to be rather inefficient in delivering kinetic energy to dense gas (Iffrig & Hennebelle 2015). When multiplying E_{SN} by a realistic efficiency factor, we see that in the weak driving case the injected turbulent energy, E_{turb}, is slightly lower or comparible to E_{SN} while in the medium driving one, E_{turb} is slightly larger than E_{SN}. This is in good agreement with the modest difference ($\simeq$ 25 per cent) found for the SFR (which will be presented in a future study) between the no driving and weak driving runs and somewhat larger one (100 per cent) found between the no-driving and medium driving runs. On the other hand, the energy injected in the strong driving case is roughly 10 times larger than in the medium driving case. While this seems a very substantial difference, let us recall that the turbulent energy dissipation is proportional to v_{rms}^3, implying that the expected rms velocity difference may only be of the order of $\simeq$2, as confirmed by the measure of the mass-weighted velocity dispersion (Table 1). This may be the reason why the coherent PS of the various driven runs present only limited differences.

5 COMPARISON TO OBSERVATIONS: THE CASE OF THE LMC

Now that we know the signature of large-scale driving on the PS decomposition, we can look for it in observations. A comparison with the Milky Way is not straightforward because we practically see it edge-on, making it difficult to observe a large-scale structure. The closest object for which suitable observations are available turns out to be the LMC. Its orientation gives it an effective depth comparable to our 1 kpc simulation box and its proximity allow for a detailed investigation of the ISM structure. We select the 500 μm observation by Herschel. The image we use has been post-processed by Gordon

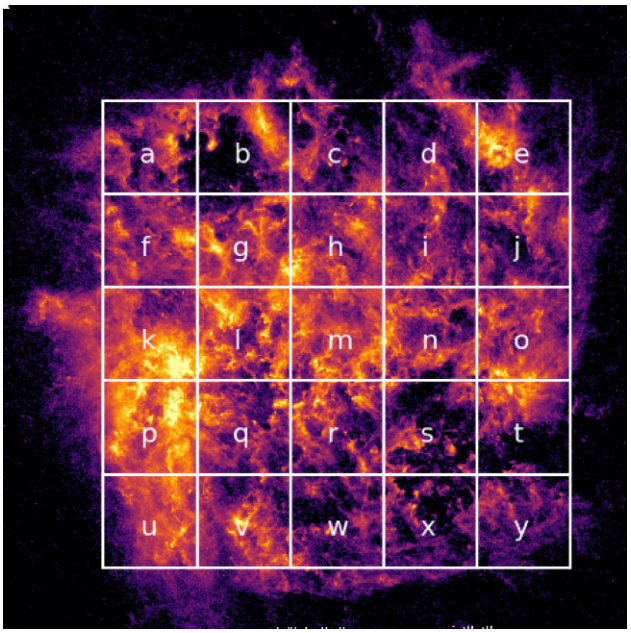

Figure 4. Image of the LMC as seen through Herschel at 500 μm and post-processed by Gordon et al. (2014). We mark a series of 1 kpc^2 regions used to compare to the simulations.

et al. (2014) and made freely available to the community.[4] At a distance of 49.6 kpc (Pietrzyński et al. 2019), the 14 arcsec observational resolution results in a physical resolution of 3.4 pc, comparable to the *physical* resolution reached for the dense gas in our simulations. The latter can be broadly estimated to be 10 times the highest resolution which is about 0.24 pc. At 500 μm, the observations trace thermal dust emission, which is well-correlated to the underlying dust density distribution. We assume the dust density to be proportional to the gas density through a constant dust-to-gas ratio.

5.1 MnGseg applied on the LMC

Before we run MnGseg on the full LMC, we cut the edges of the galaxy. The low signal-to-noise level in these regions makes the segmentation perform badly. After this, we are left with a 5×5 kpc^2 area. Unlike the simulation, the real observation is not periodic. To limit artefacts caused by the Fourrier transform, we add zero-padding of half the image size around the edges. This is necessary to avoid leakage of bright sources at the edge of the image to the other side, which would create structures that are not present in the original image and produce a false excess of large-scale power. We then perform the MnGseg on this padded 25 kpc^2. To match our simulation box, we reconstruct the PS in several 1 kpc^2 regions indicated in Fig. 4. This can be done simply by averaging $\langle|\tilde{f}_{\ell,\theta}(\vec{x})|^2\rangle_\theta$, which is outputted by MnGseg over the corresponding region. This is only possible due to the unique way in which the wavelet PS and its composition are calculated. An additional advantage of this procedure is that it significantly improves the statistics on scales between 100 and 1000 pc. Finally, we correct for the noise and Gaussian beam in the same way as in Robitaille et al. (2019):

$$P_{\rm measured}(k) = P_{\rm beam}(k) P_{\rm true}(k) + \text{noise} \tag{16}$$

[4] https://karllark.github.io/data_magclouds_dustmaps.html

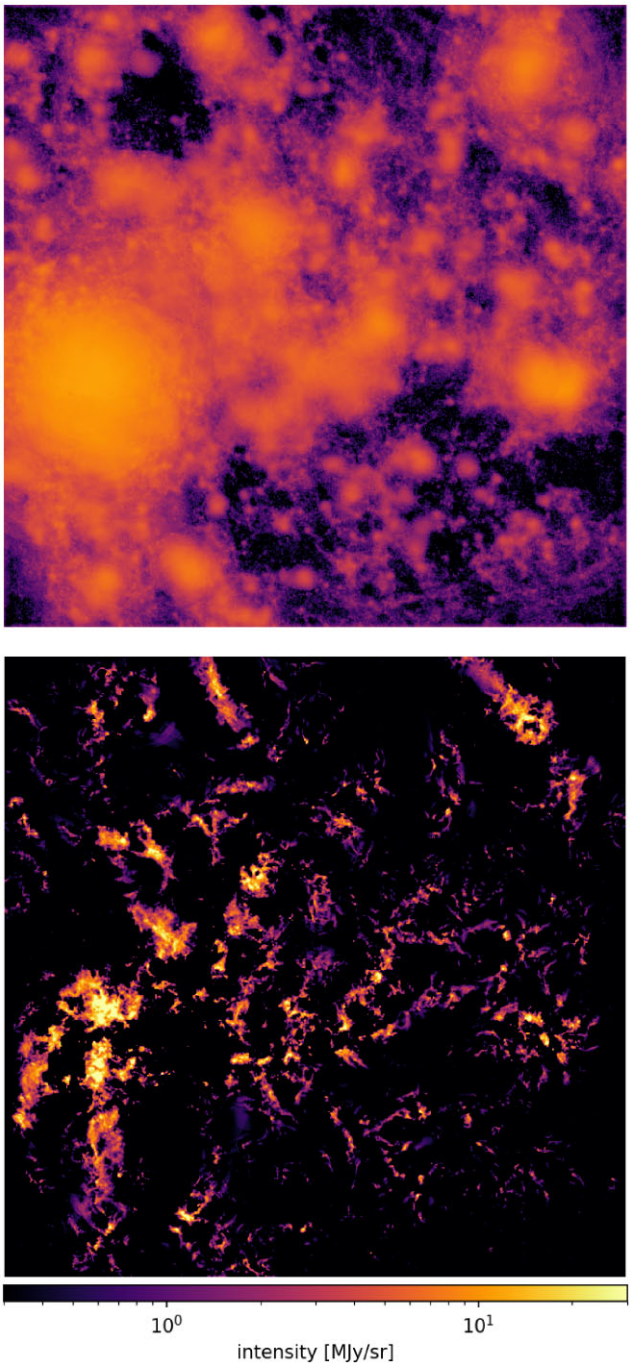

Figure 5. Image decomposition applied on the full 5×5 kpc^2 area of the LMC using $q = 2.0$. Top: Gaussian component and bottom: coherent component.

where the noise is estimated by the total PS at the smallest scale considered.

Fig. 5 shows the decomposed images obtained with $q = 2.0$. The corresponding power spectra of each 1 kpc^2 region can be found in Fig. 6. The slope is measured by fitting the same range as for the large-scale part of the simulation results. On average we measure a total PS slope of -2.13 ± 0.30 with significant variations between regions. This is in agreement with the recent study of Koch et al. (2020), who report a global index of -2.18 ± 0.05 for the full LMC, with large local variations. While the average value is roughly

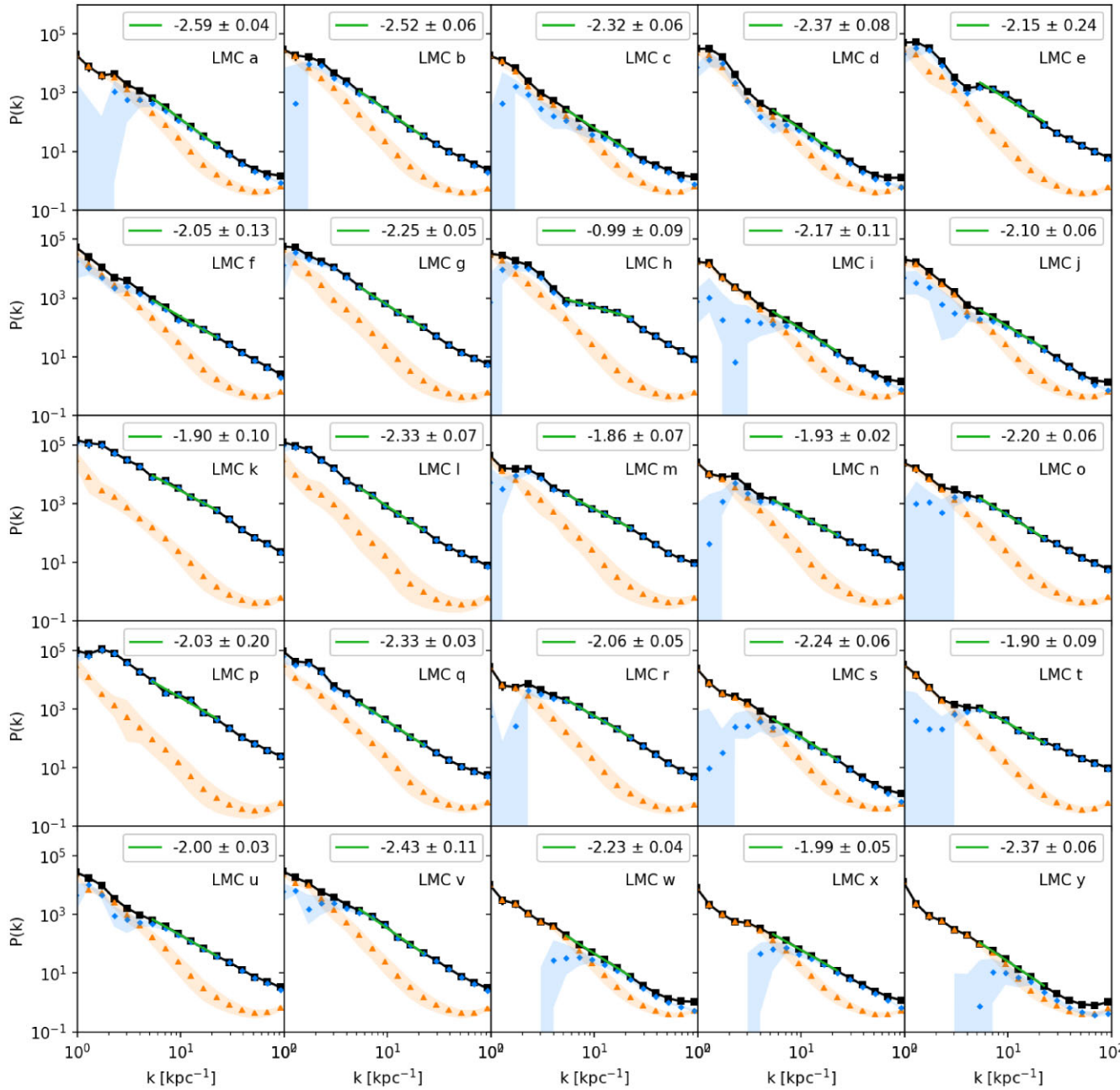

Figure 6. PS and its decomposition into Gaussian and coherent part with $q = 2.0$ for a series of 25 different 1 kpc^2 region of the LMC, extracted from the full 5 × 5 kpc^2 analysis. The green line shows a power-law fit to the total PS in the same range as the upper slope measured in the simulations. On average total PS at 1 kpc has a slope of -2.13 ± 0.30. The error bars on the total PS are smaller than the points. The maximum value of k is set by the beam size of the observation. The coloured bands show the range for the segmentation when varying q between 1.8 and 2.2.

in agreement with the medium and strong driving simulations, the differences between regions indicate that a large variety of turbulence driving mechanisms might be at play in the LMC.

5.2 Interpretation of the observed coherent PS

Fig. 7 compares the coherent PS of each LMC part with the results obtained from the simulations. The LMC PS is scaled by an arbitrary factor for easier comparison. This is necessary because 500 μm emission maps have different units than the column density maps of the simulation, and there is no straightforward conversion between the two quantities. The first important observation to make is that *none of the LMC regions matches the no-driving* simulation results. This indicates that the observed coherent structures are larger than what can be generated by stellar feedback alone. We see that for some regions the observations show a similar turn-over as for weak or medium driving case. However, many regions show a continued increase beyond any turn-over seen in the simulation results. This has several possible interpretations. The first option is that the external driving experienced by the region is stronger than what we inputted in the simulations. The fact that we do not see clear differences between the simulations with various driving strengths is an argument against this explanation. A second option is that the injection scale is larger

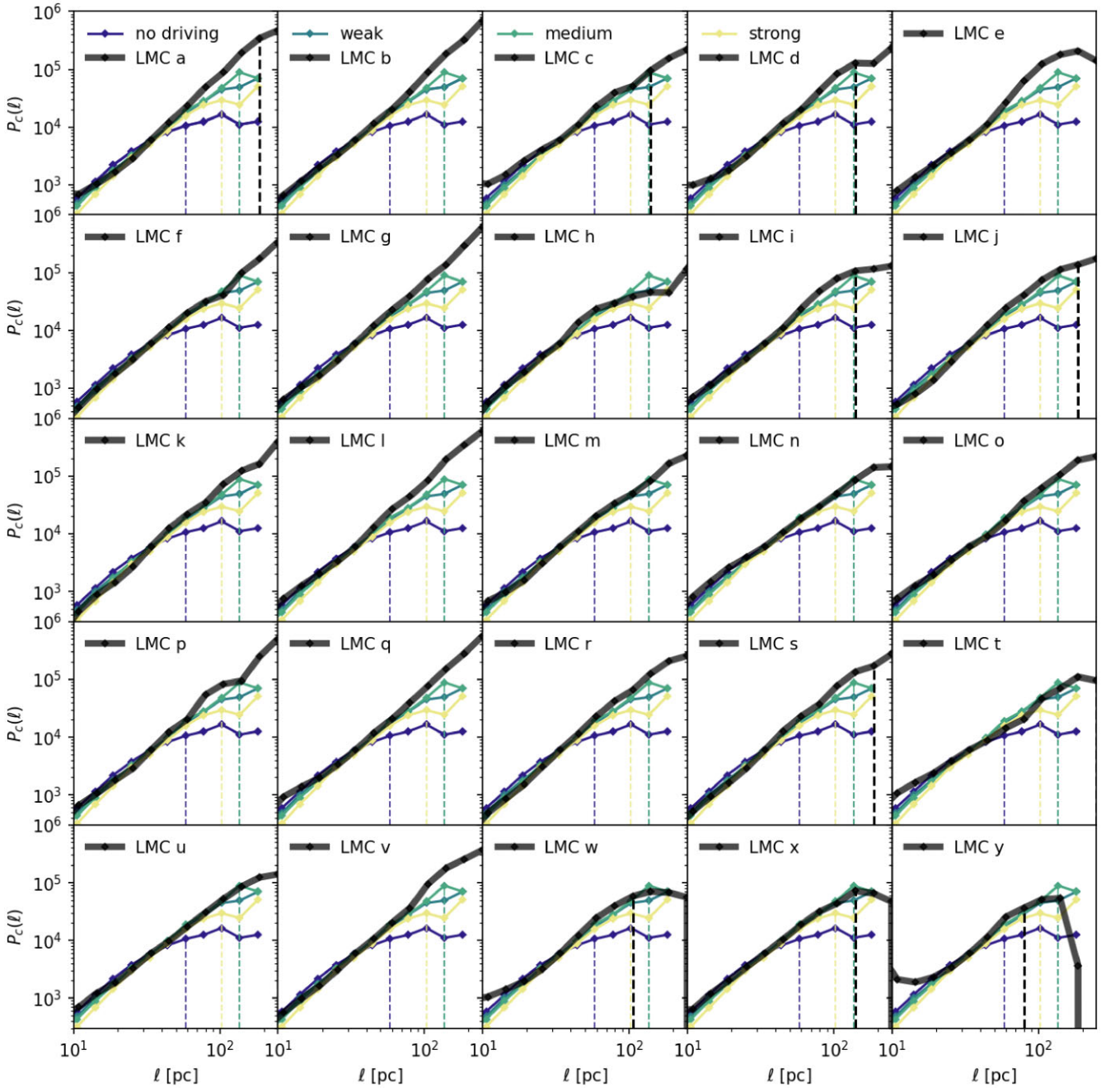

Figure 7. Comparison of the coherent PS between simulations and individual regions in the LMC. The coloured lines are the simulations for different driving strength. Each black line shows the coherent PS of the indicated LMC region scaled by an arbitrary factor to allow for easier comparison. The curved for the simulations are the same in every panel. The vertical lines mark the location of the turn-over scale $\ell_{\rm LS}$. If no vertical black line is shown, it means the turn-over in this part of the LMC occurs at scales larger than 250 pc.

than what could be studied with the simulations. Note that, while we injected turbulence on scales between 333 and 1000 pc, the statistics of the PS limit our conclusions to scales below roughly 200 pc. Since we do not vary the driving scales in our simulation suite, we cannot rule out or validate this possibility. A third option is that we underestimated the statistical error for the PS analysis of the simulations and the turn-over we see between 100 and 200 pc for the simulations with driving is caused by low statistics rather than a true decline in coherent power. This would suggest that the coherent PS for the external driving simulations follows the same increasing trend as the regions in the LMC. A last option is that the large-scale structures in the LMC are not generated by large-scale turbulence driving, but by a different physical process which was not included in the simulations. The obvious culprit here could be variations in the galactic potential. A way to test this could be to alter the background gravitational potential in our simulations to include such variations and rerun the simulation without driving. Since this work focuses on large scales, we now make the assumption that the observed structure is indeed a consequence of large-scale driving but keep in mind that this may not be valid.

Overall, these results thus seem to indicate that there is a significant large-scale turbulence driving in all regions of the LMC. The fact that the turn-over occurs on scales larger than what we reproduce in our

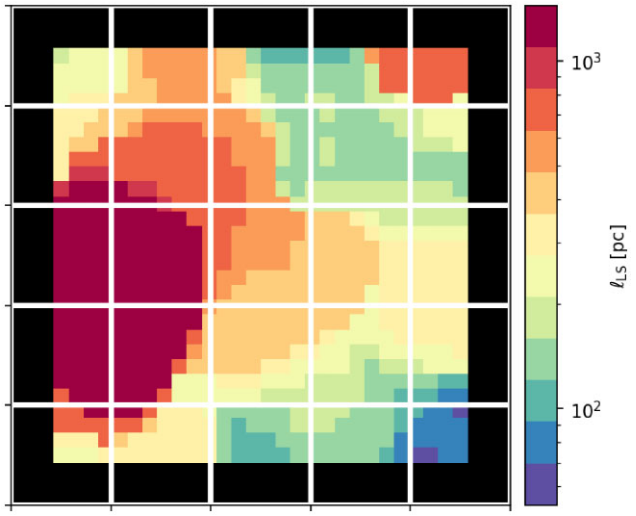

Figure 8. Map of the turn-over scale. Blue is consistent with no large-scale driving. Green shows regions consistent with values obtained from the simulations with external driving. Yellow corresponds to values around 250 pc, our statistics limit in the simulations. Orange and red indicate regions which have a turn-over scales larger than what could be measured in the simulations.

simulations seems to hint that the injection scale might be even larger than 1 kpc. Possible large-scale driving sources in the LMC will be discussed below.

5.3 Local variations of the turn-over scale

As we did for the simulations, we can measure the turn-over scale ℓ_{LS} by looking at which scales the coherent PS dominates over the Gaussian one. Using the summation method to determine the PS in 1 kpc^2 regions, we are not limited to the 25 regions we defined in Fig. 4. We can select any region we want. Pushing this philosophy to the limit, we sweep through the entire field of the LMC, shifting our 1 kpc^2 window each time by 44 pixels, resulting in 28 × 28 views spanning an area slightly less than 5 × 5 kpc^2. In each view, we reconstruct the PS and estimate the turn-over scale. Fig. 8 shows the result. Each point is centred in the 1 kpc^2 region we consider. Remark that points are correlated with their neighbours. The edges have no data (black) because we do not consider views that go outside the central 5 × 5 kpc^2 area we selected. Outside this area are the edges of the LMC and signal-to-noise ratios are poor.

Indicated with blue are the regions which have turn-over values consistent with no external turbulence driving. Only the bottom right corner matches this regime. The green regions found on the bottom, as well as a diagonal band stretching from region c-d towards i and j, have turn-over values similar to the ones obtained from the simulations with external driving (100–150 pc). Yellow marks a value of 250 pc, the upper limit for the MnGseg analysis of the simulations. Anything marked with orange or red has a coherent PS that increases beyond 300 pc. Impossible to ignore is the giant red blob on the left side of the image that marks a region around 30 Doradus, the largest and most active star formation region in the LMC (Harris & Zaritsky 2009). We will come back to this in the next section.

This map clearly hints that all regions, except a small corner, contain structures larger than what can be generated by stellar feedback alone. If we assume this large-scale structure is indeed generated by large-scale turbulence driving, then this map holds clues about which driving mechanisms operate in each part of the LMC.

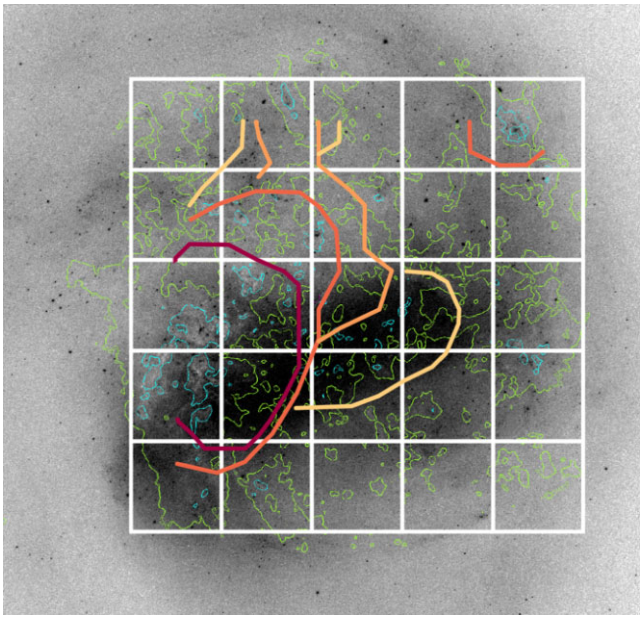

Figure 9. Stellar density map of the LMC from Gaia data release 2. The green and blue contours show the 500 μm dust emission. The orange lines mark the regions with large turn-over scale. The grid indicates the location of our 1 kpc squares.

6 DISCUSSION

6.1 Possible sources of large-scale driving

The question arises: what are the primary sources of large-scale driving? Here, we speculate based on the results obtained in the previous section for the LMC. Our goal is to give some qualitative first impressions. More models are needed to be able to make solid conclusions.

It might not seem clear at first what could be the source of a large-scale turbulence energy injection in an irregular galaxy like the LMC. However, the stellar component actually contains a bar spanning a large part of the galaxy and one spiral arm that can be seen in Fig. 9 (Harris & Zaritsky 2009; Gaia Collaboration 2018). This galactic stellar dynamic affects the gas through changes in the gravitational potential. It is possible that turbulence taps energy from this large-scale gravitational reservoir. The bar spans almost the entire width of the LMC and is located slightly below the centre of our analysis domain. Interesting observations can be made when comparing Fig. 8 to the stellar density image by Gaia (Fig. 9). To make the comparison easier, we draw orange contours which mark the main features of the turn-over scale map. The light orange diagonal patch in the centre matches well with the location of the stellar bar. Whereas any large-scale driving signature in the top corners of the image could be matched with the spiral arm, the correspondence is not as clear as for the bar.

The LMC is also tidally interacting with the SMC and the Milky Way (D'Onghia & Fox 2016; Lucchini, D'Onghia & Fox 2021; Petersen & Peñarrubia 2021). This can possibly inject energy on the full scale of the galaxy with some preferential direction. In Fig. 10, we show the large-scale environment of the LMC. The SMC is connected to the LMC through the Magellanic bridge, visible in H I. The other prominent features are the Magellanic Stream (MS), marking the trail of the orbit of the LMC and SMC around the Milky way, and the Leading Arm (LA). These structures are thought to be the result of the interaction between the LMC and SMC and the Milky Way

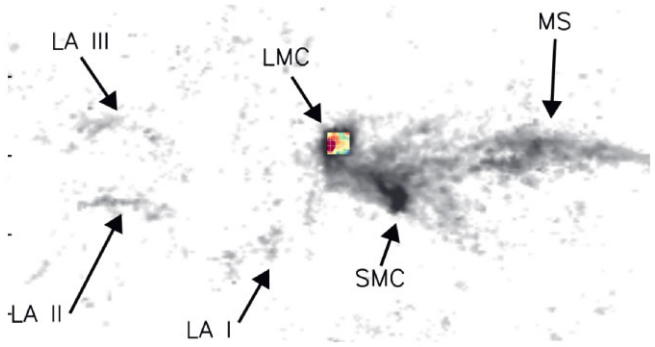

Figure 10. H I column density map from Nidever, Majewski & Butler Burton (2008), showing the interaction with the SMC, and the different parts of the LA which is due to the interaction with the Milky Way. We insert Fig. 8 at the appropriate position.

(D'Onghia & Fox 2016). Nidever et al. (2008) find that some parts of the MS and LA can be traced back to an H I overdensity in the southeast part of the LMC, where also 30 Doradus is located. This coincides with the location of the big red blob in Fig. 8 where, in our interpretation, we find a signal of turbulence driving with a very large injection scale. One interpretation of the link between the MS/LS and the starburst region 30 Doradus is that some parts of the MS and LS are created by gas outflow from extreme stellar feedback (Nidever et al. 2008). Our results show a clear correlation between large-scale driving and 30 Doradus. This can be interpreted in two (possibly more) ways: the large-scale driving mechanism generating the signal in Fig. 8 is

(1) caused by 30 Doradus itself,
(2) caused by another mechanism which possibly also created 30 Doradus, whose origin is still debated.

This brings us to the last possibility, which is the existence of supergiant shells. H II bubbles from individual stars are typically of the order of a few tens of parsec. Individual supernova bubbles are larger with total sizes of up to 100 pc. Supergiant shells are created when multiple supernova go off in close proximity of one another, combining several bubbles to generate structures of the order of several hundreds of pc and up to 1 kpc (Mac Low, McCray & Norman 1989; Chu 2008). This typically requires multiple generations of star formation. It is unclear exactly how common these are. Several super shells have been identified in the LMC in H I emission maps. In Fig. 11, we show the data from Kim et al. (1999) overlaid by our 1 kpc regions. We inspect each region and look for a link between the large-scale driving signature and the presence of a supergiant shell. The left-hand side of the image is dominated by several shells. Indeed, 30 Doradus has been identified as the source of large ionized bubbles. Any red or orange region in sections a, b, f, g, k, l, and p could be explained by a supergiant shell. Regions more in the centre of the galaxy (third column) do not contain any known supergiant shells. They do, however, show strong signs of large-scale turbulence driving. On the other hand, regions n, x, and s have bubbles but no clear signature of them in the $\ell_{\rm LS}$ map. Overall, we see that on the left-hand side of the LMC, supergiant shells could potentially be the origin of the large-scale driving. However, in the central and right-hand side, there is no clear correlation between the location of supergiant shells and large-scale driving.

These observations seem to indicate that supergiant shells alone cannot explain all of the large-scale coherent structure we see. Note that, in principle, these types of shells can form in our simulations,

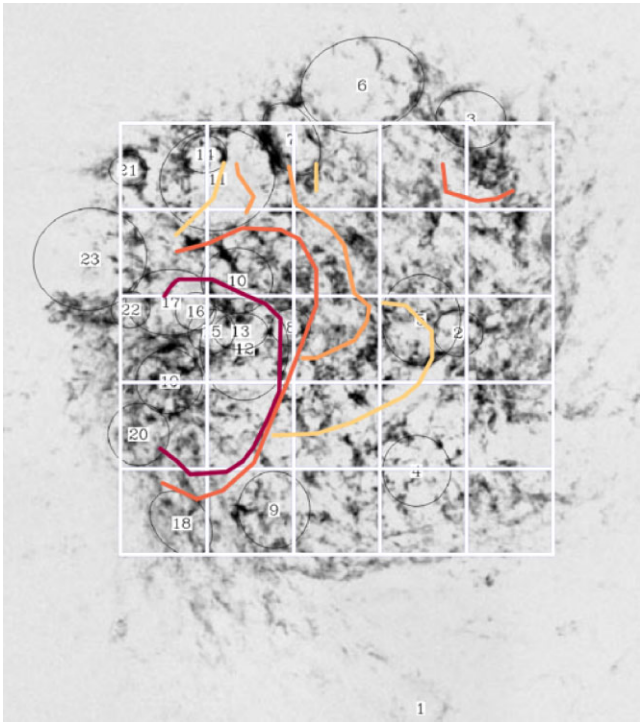

Figure 11. Approximate overlay of our selected LMC regions with the H I map and identified supergiant shells from Kim et al. (1999). The orange lines mark the regions with large turn-over scale.

since we do include supernova feedback in a self-consistent manner. In particular, supernovae explode in a correlated way since they are associated with the dense molecular clouds. So the no-driving simulation should include the signature of these supergiant shells. Intuitively, we could expect the size distribution for shells to leave an imprint on the coherent PS. If there was a sharp cut-off at a certain maximum size, we would not detect any power in the coherent PS above this scale for the no-driving simulations. The fact that we see a flattening rather than a cut-off suggests the simulations do contain several shells which are larger than the typical SN radius. There are, however, a few possible caveats that we discuss below.

6.2 Caveats related to numerical algorithms

As usual, there are many caveats related to the simulations. Our simulations have only one driving spectrum, which peaks at scales of half the box size. It is to be expected that different driving modes will create different structure sizes. The exploration of different driving modes and scales is left to future work.

Individual supernovae are not resolved in the simulation. We thus have to rely on a subgrid recipe. While extensively tested in previous simulations, a subgrid model is usually at best a reasonable approximation. It is for instance possible that our recipe is not able to reproduce a realistic number of supergiant shells, in which case it is possible that the source of the large-scale driving due to stellar feedback could be underestimated. For example, it is known that the exact location at which supernovae explode plays an important role in how efficiently it can inject energy and shape the ISM (e.g. Hennebelle & Iffrig 2014; Gatto et al. 2015). One possibility is that our recipe to estimate how far massive stars can travel from their parent cluster leads to less efficient giant shell creation. Another possibility is that a volume of 1 kpc^3 is not enough to allow for

supergiant shells to occur. Finally, our recipe only injects momentum, not energy directly, in contrast to the recipe used for instance in Kim & Ostriker (2017).

We also do not include feedback from stellar winds, because this is computationally expensive. While this might have an impact on small scales (see however Geen & de Koter 2022, who argued that winds may actually reduce the extension of H II regions), we expect the impact on large scales to be minimal.

6.3 Caveats related to the interpretation

The simulations tell us that large-scale driving generates large-scale structure. However, this does not necessarily imply that an observed large-scale structure is generated by a large-scale turbulence driving mechanism. The structure could have been generated by a process which is not present in the simulations and which leaves a similar signature on the spatial PS but does not inject additional energy to drive the turbulence. Galactic potential variations could be a candidate, though it is unclear whether or not these contribute to turbulence driving.

Using MnGseg, we can determine that there is structure of a certain size present, but we have no direct information on which process was responsible for creating it. We need to indirectly infer this by using the results from our simulations. By modelling regions with different galactic potentials, different driving scales and other variations in driving parameters, we might find more clues to explain the observations and put more constrains on the origin of structure and turbulence in the ISM. Future work that studies the turbulence cascade in full galaxy simulations will also shed more light on this matter.

Another issue is that the properties of the density field give only an indirect measure of the turbulence properties. To gain a more complete picture, the velocity field could be analysed. However, this is beyond the scope of this work.

Lastly, in purely 2D turbulence, an inverse cascade occurs due to the conservation of vorticity (Kraichnan 1967; Lazarian & Pogosyan 2000). This results in an energy PS that becomes steeper than the Kolmogorov PS for scales larger than the injection scale. This could complicate the interpretation of our results since we interpret changes of the coherent PS as a signature of the injection scale (assuming the density PS reflects the energy PS). We do not know how this inverse cascade would affect the decomposition of the PS into coherent and Gaussian part. However, the galactic disc is not a perfectly 2D structure; it has a thickness. Also, in the ISM, there are other sources of angular momentum besides the turbulence injection mechanisms. The presence of gravity and magnetic fields complicates the situation. It is unclear whether the inverse cascade can still happen under these conditions. Indeed, Hennebelle & Audit (2007) verified using 2D simulations that when the fluid is non-barotropic, as is the case in the large-scale ISM, there was no signature of an inverse cascade. On the other hand, an identical but isothermal simulation gave an energy PS much closer to the prediction from (Kraichnan 1967). In our simulations, the 2D external driving has injection scales that are already comparable to the box size. This leaves little room for an inverse cascade. The stellar feedback bubbles usually remain smaller than the disc thickness and thus are a 3D source of driving. We also do not observe a steepening of the PS at scales larger in Fig. 2, though it is possible that the effect would only be visible on scales larger than what we can analyse with our setup. On the observational side, Koch et al. (2020) show that the spatial PS of the LMC, as well as other galaxies in their sample, can be described by a single power-law without breaks. All this suggest that the inverse cascade is not important for the interpretation of our results.

6.4 Comparison to the literature

Multiple authors have studied the origin of turbulent velocities in the ISM. Using the velocity coordinate spectrum (VCS) technique, Chepurnov et al. (2010) determined the turbulence properties of a high-latitude region in the Milky Way. This technique analyses the velocity information in the H I line emission data. They derive an injection scale of 140 ± 80 pc. The big uncertainty on the result illustrates how difficult it is to study large-scale processes in the Milky Way. Stanimirović & Lazarian (2001) investigated the turbulence in the SMC, but could not identify an injection scale. They concluded that it is likely of the size of the galaxy or even larger. Later, using again the VCS technique, Chepurnov et al. (2015) indeed recovered a very large injection scale of 2.3 kpc, which implies the presence of large-scale turbulence driving, possibly due to tidal interaction with the LMC or supergiant shells. Szotkowski et al. (2019) studied spatial variations in the PS slope for both small and large scales. They find no local variations in the turbulence properties of the SMC, suggesting that stellar feedback is not the main driver. In the LMC on the other hand, they found significant variations indicating the importance of both stellar feedback and large scale processes on the turbulence. Also Besserglik & Goldman (2021) found signs of large scale driving also in the LMC. By estimating the relevant time scales, they argue that the turbulence induced by the last close passage of the SMC has not yet decayed. An example for a different galaxy can be found in a study by Dib & Burkert (2005), where they find an injection scale of about 6 kpc for the irregular galaxy Holmberg II. These findings are qualitatively in line with our analysis of the LMC, where some regions show large values of $\ell_{\rm LS}$. It is not straightforward to compare these results quantitatively, since we did not vary the injection scale in our simulations and thus cannot tell for certain how $\ell_{\rm LS}$ depends on this.

Several studies also looked for the origin of ISM turbulence in M33. Utomo, Blitz & Falgarone (2019) obtained an estimate of the turbulent energy density of roughly $1–3 \times 10^{52}$ erg pc^{-2}, which is of the same order of magnitude as our estimate for the energy injected by SN in our simulations, if we assume a low efficiency. In their work, they concluded that SN are indeed the main source of turbulence within 8 kpc. In the outer regions of the galaxy, magnetorotational instability could provide the additional energy observed. However, Koch et al. (2018) obtained a different picture, where even the combination of the two cannot explain the outer parts. Another possible source of turbulence in M33 would be due to the interaction with M31. Utomo et al. (2019) could not exclude accretion as a source when they applied the model of Klessen & Hennebelle (2010). However, the adopted parameters have large uncertainties. Interesting to note is that M33 has no bar. If bars are the main large-scale turbulence driving mechanism in the inner parts of a galaxy, we would indeed expect an energy density compatible with stellar feedback as a main driving mechanism for bar-less galaxies.

In a sample of dwarf galaxies, Stilp et al. (2013) found that star formation feedback alone is not enough to explain the observed H I kinematics and that another source of turbulence is needed to explain their data. Previous studies thus already showed that a single dominant source of turbulence is not enough to explain the observed turbulent velocities across all environments. The results in this study further support this.

7 CONCLUSIONS

In this paper, we have performed a series of four simulations describing a stratified star-forming ISM modelling a 1 kpc region of a galaxy. An external large-scale turbulence driving is applied to mimic the possible influence of large galactic scale energy injection, which we cannot self-consistently represent in our chosen computational domain. Using a MnGseg technique called MnGseg on the column density maps of our simulations, we have computed the PS of the coherent structures and the Gaussian background that MnGseg allows to separate and identify. We found that the PS of the coherent structures carries a signature of the presence of external large-scale driving. In the case where the turbulence is driven by stellar feedback only, the coherent PS is a power law that flattens above a turn-over scale of 60 pc, the typical radius of a single supernova. When external large-scale driving was included, the turn-over scale was shifted by a factor $\approx$2 to larger scales. In our simulations, external large-scale turbulence driving was thus able to create more large-scale structure than what can be created by stellar feedback alone.

We applied the same technique on 500 μm observations of the LMC, which we divided in several 1 kpc^2 regions, and found that only 1 out of 25 regions matched the results from the no-driving simulation. This result seemingly indicates that some form of large-scale turbulence driving is present in almost all parts of the LMC. To obtain clues about the nature of these driving mechanisms, we studied local various of the turn-over scale in detail. We found a particularly large turn-over scale around the starburst region 30 Doradus. This signal could be explained by a collection of supergiant shells, a form of extreme stellar feedback not observed in the simulations. Supergiant shells are also present in other regions of the LMC, but there they did not correlate with a large-scale driving signal. Also, many regions of the LMC do not contain supergiant shells and we still observed signs of large-scale driving in here. We did see a potential correlation with the stellar bar, hinting at the possible importance of galactic stellar dynamics as a turbulence driving mechanism.

The results in this work lead us to conclude that regular stellar feedback is not enough to explain the observed ISM structure on scales larger than 60 pc. Extreme feedback in the form of supergiant shells likely plays an important role but cannot explain the results in all the regions of the LMC. If we assume the ISM structure is generated by turbulence, another large-scale driving mechanism is needed to explain the entirety of the observations.

ACKNOWLEDGEMENTS

This work was granted access to HPC resources of CINES and CCRT under the allocation x2020047023 made by Grand Equipement National de Calcul Intensif (GENCI). This research has received funding from the European Research Council synergy grant ECOGAL (grant 855130). TC would like to thank all the members of the ECOGAL collaboration for discussions and comments which greatly improved this work. This work also benefited from the Grand Cascade workshop hosted at Institute Pascal in Orsay, France. TC would also like to thank Steve Longmore for teaching her how to use Aladin during the Advanced School on Star formation in Granada. RSK and SCOG acknowledge funding from the German Research Foundation (DFG) under Germany's Excellence Strategy for the STRUCTURES cluster of excellence in Heidelberg (EXC-2181/1 - 390900948) and also via the collaborative research center (SFB 881, Project-ID 138713538) 'The Milky Way System' (subprojects A1, B1, B2, and B8). LT acknowledges funding from the Italian Ministero dell'Istruzione, Università e Ricerca through the grant Progetti Premiali 2012 - iALMA (CUP C52I13000140001), from the Deutsche Forschungs-gemeinschaft (DFG, German Research Foundation) - Ref no. 325594231 FOR 2634/1 TE 1024/1-1, from the DFG ORIGINS cluster of excellence in Munich (www.origins-cluster.de), and from he European Union's Horizon 2020 research and innovation programme under the Marie Sklodowska-Curie grant agreement No 823823 (DUSTBUSTERS).

DATA AVAILABILITY

The data underlying this article are available in the Galactica database at http://www.galactica-simulations.eu/db/STAR_FORM/LS_DRIVING/ . All analysis scripts used to produce the figures in this work are available at https://bitbucket.org/TineColman/apophis/. in the directory `Paper_Colman_et_al2022`.

REFERENCES

Audit E., Hennebelle P., 2005, A&A, 433, 1
Avillez M. A., Breitschwerdt D., 2005, A&A, 436, 585
Bate M. R., Bonnell I. A., Price N. M., 1995, MNRAS, 277, 362
Besserglik D., Goldman I., 2021, ApJ, 915, 117
Bleuler A., Teyssier R., 2014, MNRAS, 445, 4015
Bleuler A., Teyssier R., Carassou S., Martizzi D., 2015, Comput. Astrophys. Cosmol., 2, 5
Bournaud F., Elmegreen B. G., Teyssier R., Block D. L., Puerari I., 2010, MNRAS, 409, 1088
Brucy N., Hennebelle P., Bournaud F., Colling C., 2020, ApJ, 896, L34
Chepurnov A., Burkhart B., Lazarian A., Stanimirovic S., 2015, ApJ, 810, 33
Chepurnov A., Lazarian A., Stanimirović S., Heiles C., Peek J. E. G., 2010, ApJ, 714, 1398
Chu Y.-H., 2008, in Bresolin F., Crowther P. A., Puls J., eds, Massive Stars as Cosmic Engines, Vol. 250, Cambridge University Press, p. 341
Colling C., Hennebelle P., Geen S., Iffrig O., Bournaud F., 2018, A&A, 620, A21
D'Onghia E., Fox A. J., 2016, ARA&A, 54, 363
Dib S., Burkert A., 2005, ApJ, 630, 238
Elmegreen B. G., Kim S., Staveley-Smith L., 2001, ApJ, 548, 749
Elmegreen B. G., Scalo J., 2004, ARA&A, 42, 211
Eswaran V., Pope S. B., 1988, Comput. Fluids, 16, 257
Falgarone E., Hily-Blant P., Levrier F., 2004, Ap&SS, 292, 89
Federrath C., Banerjee R., Clark P. C., Klessen R. S., 2010b, ApJ, 713, 269
Federrath C., Klessen R. S., 2013, ApJ, 763, 51
Federrath C., Klessen R. S., Schmidt W., 2008, ApJ, 688, L79
Federrath C., Roman-Duval J., Klessen R. S., Schmidt W., Mac Low M. M., 2010a, A&A, 512, A81
Fromang S., Hennebelle P., Teyssier R., 2006, A&A, 457, 371
Gaensler B. M., Haverkorn M., Staveley-Smith L., Dickey J. M., McClure-Griffiths N. M., Dickel J. R., Wolleben M., 2005, Science, 307, 1610
Gaia Collaboration, 2018, A&A, 616, A12
Gatto A. et al., 2015, MNRAS, 449, 1057
Geen S., de Koter A., 2022, MNRAS, 509, 4498
Geen S., Hennebelle P., Tremblin P., Rosdahl J., 2016, MNRAS, 463, 3129
Girichidis P. et al., 2016, MNRAS, 456, 3432
Gordon K. D. et al., 2014, ApJ, 797, 85
Harris J., Zaritsky D., 2009, AJ, 138, 1243
Hassani H., Tabatabaei F., Hughes A., Chastenet J., McLeod A. F., Schinnerer E., Nasiri S., 2022, MNRAS, 510, 11
Hennebelle P., Audit E., 2007, A&A, 465, 431
Hennebelle P., Falgarone E., 2012, A&AR, 20, 55
Hennebelle P., Iffrig O., 2014, A&A, 570, A81
Iffrig O., Hennebelle P., 2015, A&A, 576, A95
Iffrig O., Hennebelle P., 2017, A&A, 604, A70
Jin K., Salim D. M., Federrath C., Tasker E. J., Habe A., Kainulainen J. T., 2017, MNRAS, 469, 383

Joung M. K. R., Mac Low M.-M., 2006, ApJ, 653, 1266
Kennicutt R. C., Evans N. J., 2012, ARA&A, 50, 531
Kim C.-G., Ostriker E. C., 2017, ApJ, 846, 133
Kim C.-G., Ostriker E. C., Kim W.-T., 2013, ApJ, 776, 1
Kim S., Dopita M. A., Staveley-Smith L., Bessell M. S., 1999, AJ, 118, 2797
Kim S., Staveley-Smith L., Dopita M. A., Sault R. J., Freeman K. C., Lee Y., Chu Y.-H., 2003, ApJS, 148, 473
Kirby J. F., 2005, Comput. Geosci., 31, 846
Klessen R. S., Glover S. C. O., 2016, Saas-Fee Adv. Course, 43, 85
Klessen R. S., Hennebelle P., 2010, A&A, 520, A17
Koch E. W. et al., 2018, MNRAS, 479, 2505
Koch E. W., Chiang I.-D., Utomo D., Chastenet J., Leroy A. K., Rosolowsky E. W., Sandstrom K. M., 2020, MNRAS, 492, 2663
Kraichnan R. H., 1967, Phys. Fluids, 10, 1417
Kritsuk A. G., Norman M. L., Padoan P., Wagner R., 2007, ApJ, 665, 416
Krumholz M. R., Burkhart B., Forbes J. C., Crocker R. M., 2018, MNRAS, 477, 2716
Kuijken K., Gilmore G., 1989, MNRAS, 239, 605
Lazarian A., Pogosyan D., 2000, ApJ, 537, 720
Lesieur M., 2008, Turbulence in Fluids. Springer, Berlin
Lucchini S., D'Onghia E., Fox A. J., 2021, ApJ, 921, L36
Mac Low M.-M., Klessen R. S., 2004, Rev. Mod. Phys., 76, 125
Mac Low M.-M., McCray R., Norman M. L., 1989, ApJ, 337, 141
McKee C. F., Ostriker E. C., 2007, ARA&A, 45, 565
Meidt S. E. et al., 2018, ApJ, 854, 100
Miville-Deschênes M. A., Lagache G., Boulanger F., Puget J. L., 2007, A&A, 469, 595
Nguyen van yen R., Farge M., Schneider K., 2012, Phys. D Nonlinear Phenom., 241, 186
Nidever D. L., Majewski S. R., Butler Burton W., 2008, ApJ, 679, 432
Nusser A., Silk J., 2022, MNRAS, 509, 2979
Padoan P., Pan L., Haugbølle T., Nordlund Å., 2016, ApJ, 822, 11
Petersen M. S., Peñarrubia J., 2021, Nature Astron., 5, 251
Pietrzyński G. et al., 2019, Nature, 567, 200
Renaud F., Kraljic K., Bournaud F., 2012, ApJ, 760, L16
Robitaille J. F., Joncas G., Miville-Deschênes M. A., 2014, MNRAS, 440, 2726
Robitaille J. F., Motte F., Schneider N., Elia D., Bontemps S., 2019, A&A, 628, A33
Rosdahl J., Blaizot J., Aubert D., Stranex T., Teyssier R., 2013, MNRAS, 436, 2188
Salpeter E. E., 1955, ApJ, 121, 161
Schmidt W., Federrath C., Hupp M., Kern S., Niemeyer J. C., 2009, A&A, 494, 127
Schmidt W., Niemeyer J. C., Hillebrandt W., 2006, A&A, 450, 265
Schneider N. et al., 2015, MNRAS, 453, L41
Stanimirović S., Lazarian A., 2001, ApJ, 551, L53
Stilp A. M., Dalcanton J. J., Skillman E., Warren S. R., Ott J., Koribalski B., 2013, ApJ, 773, 88
Szotkowski S. et al., 2019, ApJ, 887, 111
Teyssier R., 2002, A&A, 385, 337
Utomo D., Blitz L., Falgarone E., 2019, ApJ, 871, 17
Wada K., 2008, ApJ, 675, 188
Walch S. et al., 2015, MNRAS, 454, 238
Wong T. et al., 2011, ApJS, 197, 16
Woosley S. E., Heger A., Weaver T. A., 2002, Rev. Mod. Phys., 74, 1015

SUPPORTING INFORMATION

Supplementary data are available at *MNRAS* online.

Appendix A. How MnGseg works.
Appendix B. Varying the q parameter for segmentation.
Appendix C. Padding and apodizing.
Appendix D. Statistical stationarity.

Please note: Oxford University Press is not responsible for the content or functionality of any supporting materials supplied by the authors. Any queries (other than missing material) should be directed to the corresponding author for the article.

This paper has been typeset from a TEX/LATEX file prepared by the author.